

REPORT

OPTICAL CLOCKS

A Fermi-degenerate three-dimensional optical lattice clock

S. L. Campbell,^{1,2*} R. B. Hutson,^{1,2*} G. E. Marti,¹ A. Goban,¹ N. Darkwah Oppong,^{1†} R. L. McNally,^{1,2‡} L. Sonderhouse,^{1,2} J. M. Robinson,^{1,2} W. Zhang,^{1§} B. J. Bloom,^{1,2||} J. Ye^{1,2¶}

Strontium optical lattice clocks have the potential to simultaneously interrogate millions of atoms with a high spectroscopic quality factor of 4×10^{17} . Previously, atomic interactions have forced a compromise between clock stability, which benefits from a large number of atoms, and accuracy, which suffers from density-dependent frequency shifts. Here we demonstrate a scalable solution that takes advantage of the high, correlated density of a degenerate Fermi gas in a three-dimensional (3D) optical lattice to guard against on-site interaction shifts. We show that contact interactions are resolved so that their contribution to clock shifts is orders of magnitude lower than in previous experiments. A synchronous clock comparison between two regions of the 3D lattice yields a measurement precision of 5×10^{-19} in 1 hour of averaging time.

Atomic clocks are advancing the frontier of measurement science, enabling tabletop searches for dark matter and physics beyond the Standard Model (1–4), as well as providing innovative quantum technologies for other branches of science (5). One-dimensional (1D) optical lattice clocks provide a many-particle optical frequency reference that, together with advances in optical local oscillators, has led to record clock stability (6, 7) and the accompanying ability to evaluate systematic shifts with greater accuracy than ever before (8–12). However, the need to avoid atomic interactions places increasingly challenging engineering constraints on 1D optical lattice systems (13–15). A 3D optical lattice was used in (16) to suppress atomic interactions in a clock based on a thermal gas of bosons. As the next step, the tools developed for quantum gas research (17–21) can be used to prepare metrologically useful quantum matter, combining the benefits of single-particle quantum state control and correlated many-particle systems.

We used these tools to implement a 3D optical lattice clock with a degenerate Fermi gas. In this configuration, the number of atoms can in principle be scaled by orders of magnitude, whereas strong interactions prevent systematic errors associated with high atomic density. Specifically,

we loaded a two-spin degenerate Fermi gas into the ground band of a 3D optical lattice in the Mott insulating regime, where interactions are responsible for a suppression of doubly occupied sites (18, 19, 21). This enabled us to maximize atomic density while greatly suppressing collisional frequency shifts. For our coldest samples, the number of doubly occupied sites was suppressed by orders of magnitude relative to the expected value for a noninteracting gas (22). For any residual atoms in doubly occupied sites, the enhanced interaction energy in a 3D lattice ensures that their transitions are well resolved from the unperturbed clock transitions for atoms in singly occupied sites. Consequently, we were able to operate at a density above 10^{13} atoms/cm³, three orders of magnitude greater than in previous lattice clock experiments (10).

Laser cooling followed by optical pumping to the $m_F = \pm 9/2$ stretched nuclear spin states (where m_F is the projection of the total angular momentum F along the quantization axis) produced a two-spin Fermi gas with an initial phase space density of 0.1 in a crossed optical dipole trap (XODT). Evaporative cooling to degeneracy proceeded by exponentially decreasing the trap depth in a 7-s, two-stage ramp (23, 24). For different measurement goals, we optimized particular final parameters such as temperature (10 to 60 nK) and number of atoms (10^4 to 10^5). The temperature T and Fermi temperature T_F were determined from a fit of a freely expanding gas to the Fermi-Dirac distribution, giving $T/T_F = 0.2$ to 0.3.

The atoms were then adiabatically loaded from the XODT into the ground band of a 3D optical lattice. We experimentally verified adiabaticity by measuring that T/T_F did not increase by more than 10% after round-trip loading back into the XODT. As the lattice depth rose, the

increasing role of interactions relative to tunneling suppressed multiple occupancies in the Mott insulating regime. At the final lattice depths of 40 to 100 E_{rec} , where E_{rec} is the lattice photon recoil energy, the Lamb-Dicke requirement was satisfied for clock light along all directions (25). Spectroscopy was performed on the 698-nm $^1S_0(|g; m_F\rangle) \leftrightarrow ^3P_0(|e; m_F\rangle)$ clock transition. The clock laser propagating along the \hat{x} lattice beam was used for precision spectroscopy (Fig. 1A), whereas an oblique clock laser enabled a systematic characterization of the lattice by means of motional sideband spectroscopy (Fig. 1B). The absence of observable red-detuned sidebands demonstrated that the atoms were predominantly loaded into the ground band of the 3D lattice.

A long-standing question has been whether the overall ac Stark shift in a 3D lattice can be managed to allow state-of-the-art narrow-line clock spectroscopy. We implemented a solution to this challenge, inspired by the proposal in (26). The differential ac Stark shift from the lattice trapping beams at a particular trap depth U_0 can be expressed in terms of its scalar, vector, and tensor components as

$$\Delta\nu = (\Delta\kappa^s + \Delta\kappa^v m_F \xi \hat{e}_k \cdot \hat{e}_B + \Delta\kappa^t \beta) U_0 \quad (1)$$

where $\Delta\kappa^{\text{svt}}$ are the scalar, vector, and tensor shift coefficients, respectively; ξ is the lattice light ellipticity; and \hat{e}_k and \hat{e}_B are unit vectors along the lattice beam wave vector and magnetic field quantization axis, respectively (26, 27). The parameter β can be expressed as $\beta = (3\cos^2\theta - 1)[3m_F^2 - F(F+1)]$, where θ is the angle between the nearly linear lattice polarization and \hat{e}_B .

We achieved state-independent trapping by operating the lattice at the combined scalar and tensor magic frequency and ensuring that the vector shift was zero (10, 28). Linearly polarized lattice light ($\xi = 0$) suppressed the vector shift, and the tensor shift was minimally sensitive to drifts in θ by using polarizations either parallel ($\theta = 0^\circ$) or perpendicular ($\theta = 90^\circ$) to the quantization axis. The frequency of the trapping light was then tuned to adjust the scalar shift so that it precisely canceled the tensor component. The $\theta = 0^\circ$ configuration has been thoroughly studied in 1D lattice clocks (10, 28). For the 3D lattice, we set the horizontal (\hat{x}, \hat{y}) and vertical (\hat{z}) lattice polarizations to be parallel and perpendicular to \hat{e}_B , respectively (Fig. 1A). The two polarization configurations had distinct magic frequencies owing to their different tensor shifts.

We measured the magic frequencies for the vertical and horizontal lattice beams. A continuous-wave Ti:sapphire laser was used for the lattice light because of its low incoherent background (29). The absolute frequency of the lattice laser was traceable to the coordinated universal time scale maintained at NIST through an optical frequency comb. For a given lattice laser frequency, we measured the differential ac Stark shift using four interleaved digital servos that locked the clock laser frequency to the atomic resonance for alternating high and low lattice intensities and $m_F = \pm 9/2$ spin states (8, 10, 28). From the data

¹JILA, National Institute of Standards and Technology (NIST) and University of Colorado Boulder, 440 UCB, Boulder, CO 80309, USA. ²Department of Physics, University of Colorado Boulder, 390 UCB, Boulder, CO 80309, USA.

*These authors contributed equally to this work. †Present address: Max-Planck-Institut für Quantenoptik, Hans-Kopfermann-Straße 1, 85748 Garching, Germany. ‡Present address: Department of Physics, Columbia University, 538 West 120th Street, New York, NY 10027-5255, USA. §Present address: NIST, 325 Broadway, Boulder, CO 80305, USA. ||Present address: Rigetti Computing, 775 Heinz Avenue, Berkeley, CA 94710, USA.

¶Corresponding author. Email: ye@jila.colorado.edu

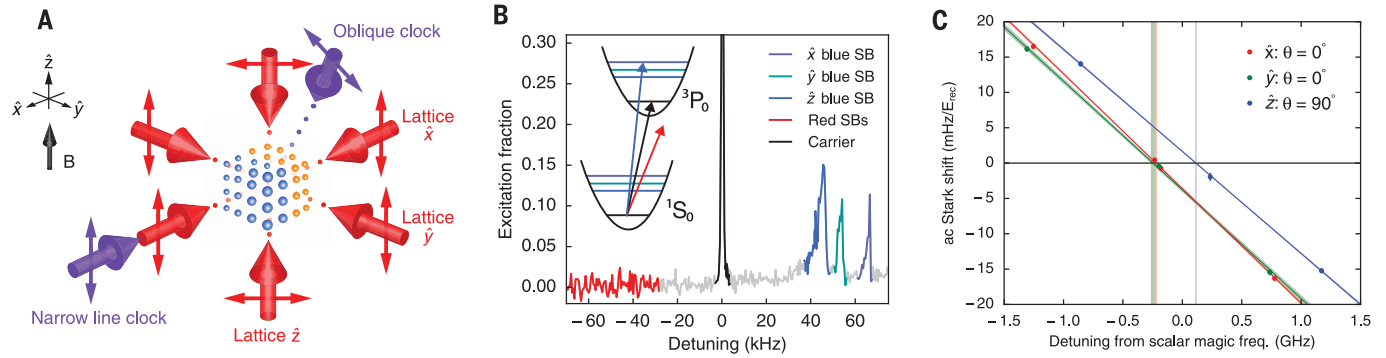


Fig. 1. 3D optical lattice configuration and motional state characterization. (A) Schematic showing the propagation direction (large arrows) and polarization (double arrows) of the 3D lattice and clock laser beams. The quantization axis is defined by the magnetic field B . The narrow-line clock laser used for precision spectroscopy is phase-stabilized to lattice \hat{x} . The oblique clock laser is used to drive motional sidebands along all three lattice axes. (B) Motional sideband spectroscopy using the oblique clock laser shows no observable red sidebands (SBs), illustrating that atoms are predominantly in

the ground band of the lattice. (C) Determination of the magic frequencies for the horizontal (\hat{x}, \hat{y}) and vertical (\hat{z}) lattices, with $m_F = \pm 9/2$. The measured frequency shift (filled circles with 1σ error bars) is scaled by the difference in trap depths between the high and low lattice intensities (22). Linear fits to the data are shown by opaque lines, with 1σ statistical uncertainties shown as shaded regions. The difference in the slopes is caused by trapping potential inhomogeneities that do not affect the determination of the magic frequencies (1σ uncertainties indicated by the vertical shaded regions).

shown in Fig. 1C, we determined that the vertical ($\theta = 90^\circ$) and horizontal ($\theta = 0^\circ$) magic frequencies were 368.554839(5) and 368.554499(8) THz, respectively, in agreement with (10, 28, 29). From these two magic frequencies, we found that the scalar magic frequency was 368.554726(4) THz, in agreement with (29).

Because there are only two θ configurations with a stable tensor shift, in a 3D lattice, two of the three lattice beams will necessarily have the same magic frequency. However, the frequencies of all lattice beams must be offset to avoid interference, which is known to cause heating in ultracold quantum gas experiments (30). We chose our two horizontal beams to have the same polarization and operated them with equal and opposite detunings (± 2.5 MHz) from their magic frequency, giving equal and opposite ac Stark shifts from the two beams. From the slopes in Fig. 1C, we determined that for a 10% imbalance in trap depths, detuning the two horizontal beams ± 2.5 MHz from their magic frequency would result in a systematic shift of $< 1 \times 10^{-18}$, the exact magnitude of which can be measured to much better accuracy.

Another issue resulting from our 3D geometry is that one lattice beam must operate with $\hat{e}_k \cdot \hat{e}_B = 1$, which can give rise to a vector ac Stark shift owing to residual circular polarization. The vertical (\hat{z}) beam has this configuration, and we measured a vector shift of $3 \times 10^{-18} \times m_F/E_{\text{rec}}$ (22), corresponding to an ellipticity of $\xi = 0.007$ (26). In contrast, the horizontal beams (\hat{x}, \hat{y}) with $\hat{e}_k \cdot \hat{e}_B = 0$ enjoy an additional level of vector shift suppression. Because the clock operates by locking to alternating opposite spin states, the net vector shift can be removed.

In the ground band of the lattice, each site can be occupied by either one atom or two atoms with opposite nuclear spin. Tight confinement in the 3D lattice gives rise to strong interactions on doubly occupied sites. We label the two-

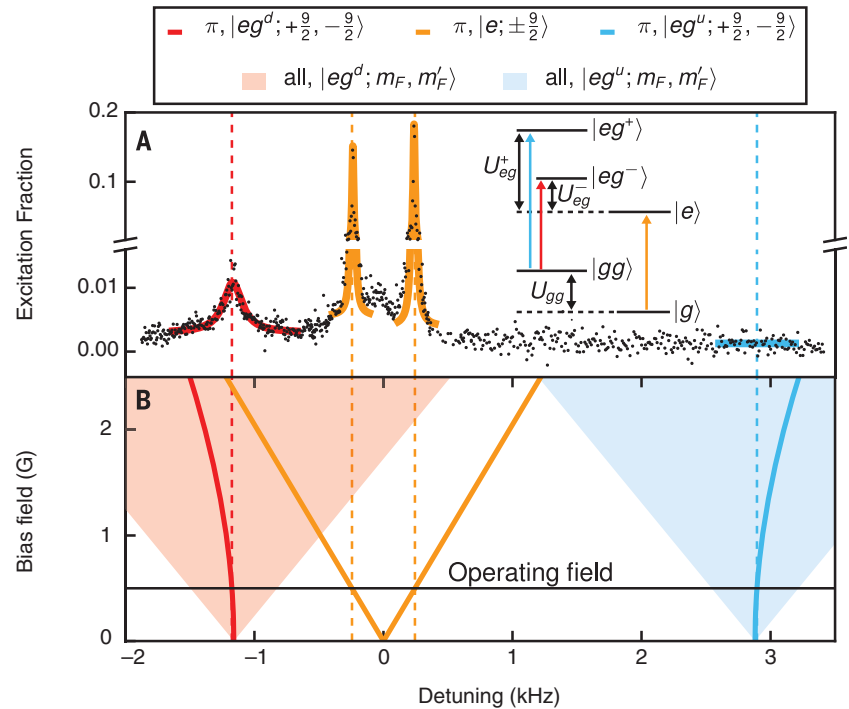


Fig. 2. Resolved atomic contact interactions. (A) Clock spectroscopy data for a two-spin Fermi gas in the $m_F = \pm 9/2$ stretched states for a 500-mG magnetic field, where a small fraction of the lattice sites contain both spin states. All transitions are saturated. The $|gg; m_F, m'_F\rangle \rightarrow |eg^u; m_F, m'_F\rangle$ transition is absent owing to its vanishing dipole matrix element at small magnetic fields. Inset, level diagram at zero magnetic field. (B) Calculated detunings for transitions on singly and doubly occupied sites (22). The solid lines correspond to transitions on singly occupied (orange) and doubly occupied (red and blue) sites with $m_F = \pm 9/2$. Transitions on doubly occupied sites for arbitrary m_F and clock laser polarization lie within the shaded regions. At our operating magnetic field of 500 mG, all resonances for doubly occupied sites are well resolved from the clock transitions.

particle eigenstates of the two-orbital interaction Hamiltonian as $|gg; m_F, m'_F\rangle = |gg\rangle \otimes |s\rangle$, $|eg^+; m_F, m'_F\rangle = (|eg\rangle + |ge\rangle)/\sqrt{2} \otimes |s\rangle$, $|eg^-; m_F, m'_F\rangle = (|eg\rangle - |ge\rangle)/\sqrt{2} \otimes |t\rangle$, and $|ee; m_F, m'_F\rangle = |ee\rangle \otimes |s\rangle$ with corresponding energies $U_{gg}, U_{eg^+}, U_{eg^-}$, and

U_{ee} (31–34). Here $|s\rangle$ and $|t\rangle$ represent the singlet and triplet wave functions for the two spins, m_F and m'_F . An applied magnetic bias field mixes the $|eg^+; m_F, m'_F\rangle$ and $|eg^-; m_F, m'_F\rangle$ states owing to a difference between the Landé

g -factors of the two orbitals. We label the new eigenstates of the combined interaction and Zeeman Hamiltonian $|eg^u; m_F, m'_F\rangle$ and $|eg^d; m_F, m'_F\rangle$.

Clock light resonantly couples the ground state $|gg; m_F, m_F\rangle$ only to the states $|eg^{u,d}; m_F, m'_F\rangle$. The energies U_{eg^+} and U_{eg^-} differ from U_{gg} on the h -kilohertz scale, where h is the Planck constant, resulting in transitions on doubly occupied sites that are well resolved from the single-atom clock transitions and strong suppression of two-photon transitions to the $|ee; m_F, m'_F\rangle$ state. In 1D optical lattice clocks, interaction shifts are less than clock transition Rabi frequencies; in 2D clocks, interaction shifts and Rabi frequencies are comparable (35). In contrast, the interaction shifts in a 3D lattice are 10^3 times the clock transition Rabi frequency. Although for normal clock operation, we loaded at most one atom per site, to measure contact interactions, we increased the final Fermi temperature so that a small fraction of lattice sites were filled with two atoms in the $|gg; m_F, m'_F\rangle$ state. Figure 2A shows clock spectroscopy for a magnetic field $B = 500$ mG. At this field, π -polarized clock light produced a negligible transition amplitude to the $|eg^u; m_F, m'_F\rangle$ state thanks to destructive interference between the two oppositely signed transition dipole moments for the stretched states. Therefore, we observed excitation to the $|eg^d; m_F, m'_F\rangle$ state (red) and no excitation to the $|eg^u; m_F, m'_F\rangle$ state (blue).

Clock operation predominantly probes atoms in singly occupied sites, with only a negligible systematic shift due to line pulling caused by transitions from the few atoms in doubly occupied sites. For a comprehensive study of line pulling from doubly occupied sites, we used our measurements of $U_{eg^-} - U_{gg}$ and $U_{eg^+} - U_{gg}$ at $B = 0$ to calculate the spectrum of all transitions on doubly occupied sites as a function of B (Fig. 2B) (22). We accounted for imperfect clock laser polarization and residual spin populations by considering transitions to all $|eg^{u,d}; m_F, m'_F\rangle$ states for both linearly and circularly polarized light, as indicated in the shaded regions in Fig. 2B. At intermediate magnetic fields, transitions from doubly occupied sites can cross clock transitions and potentially cause substantial frequency shifts. However, this is avoided if B is kept sufficiently low. At our chosen bias field of 500 mG (8, 10), transitions on doubly occupied sites were at least 500 Hz away. From a 1% upper bound on residual transition amplitudes, we estimated the fractional frequency shift caused by line pulling from doubly occupied sites to be below 1×10^{-24} for 1-Hz linewidths (22). We also calculated the fractional frequency shifts coming from superexchange interactions (36) between neighboring sites at typical lattice depths and found them to be below 1×10^{-22} .

Although on-site interaction shifts can be eliminated in 3D lattice clocks, atoms may also interact through long-range electric dipole forces, which can lead to many-body effects such as collective frequency shifts, superradiance, and subradiance (37). At unit filling, clock shifts from dipolar interactions could reach the 10^{-18} level,

although using different 3D lattice geometries is a promising approach for canceling these shifts (38, 39). Exploring different strategies for accurately measuring and eliminating dipolar frequency shifts will be a fruitful avenue of future study.

With atomic interactions and lattice ac Stark shifts controlled, we demonstrate the longest coherence times in atom-light interactions. Figure 3 shows a progression of Ramsey fringes with free evolution times from 100 ms to 6 s, beyond what has been demonstrated in 1D lattice clocks (10, 15, 40). The \hat{x} lattice beam was operated at a depth ($>80E_{\text{rec}}$) sufficient to prevent atoms from tunneling along the clock laser axis during the 6-s free evolution period. Spectroscopy was performed on a spin-polarized sample, prepared by first exciting $|g; -9/2\rangle \rightarrow |e; -9/2\rangle$, then removing all ground state atoms by means of resonant $^1S_0 \rightarrow ^1P_1$ light. Our longest observed coherence time approached the limit of our clock laser based on its noise model (41) and the 12.7-s dead time between measurements. For the demonstration of Ramsey fringes at longer free evolution times, maintaining atom-light phase coherence will require a substantial reduction in fundamental thermal noise from the optical local oscillator. Additionally, the observation of narrower lines will require magnetic field control below the 100- μ G level. The contrast of the observed Ramsey fringes was likely limited by lattice light causing both dephasing over the atomic sample and excited-state population decay. The external harmonic confine-

ment of the lattice beams limited the size of the Mott insulating region in the center of the trap to $\sim 2 \times 10^4$ atoms. We maximized the number of singly occupied sites in the center of the trap by operating with 1×10^4 atoms at a temperature of 15 nK.

The combination of large numbers of atoms and a long atom-light coherence time enabled by this system opens the possibility of improving the quantum projection noise (QPN) limit on clock stability by more than an order of magnitude over the current state of the art (10, 40). The QPN limit for Ramsey spectroscopy is

$$\sigma_{\text{QPN}}(\tau) = \frac{1}{2\pi\nu T_R} \sqrt{\frac{T_R + T_d}{N\tau}} \quad (2)$$

where ν is the clock frequency, T_R is the free evolution time, T_d is the dead time, and τ is the total averaging time. Typically, optical clocks operate at a stability above this limit owing to the Dick effect (42). However, operation at or near the QPN limit has recently been demonstrated in a number of different systems; common-mode rejection of clock laser noise has been achieved through synchronous interrogation of two independent atomic ensembles (6, 43) and two separated ions in a single ion trap (44), whereas interleaved interrogation of two clocks with zero dead time has enabled continuous monitoring of the clock laser phase (40).

Here we demonstrate synchronous clock comparison between two spatially separated atomic

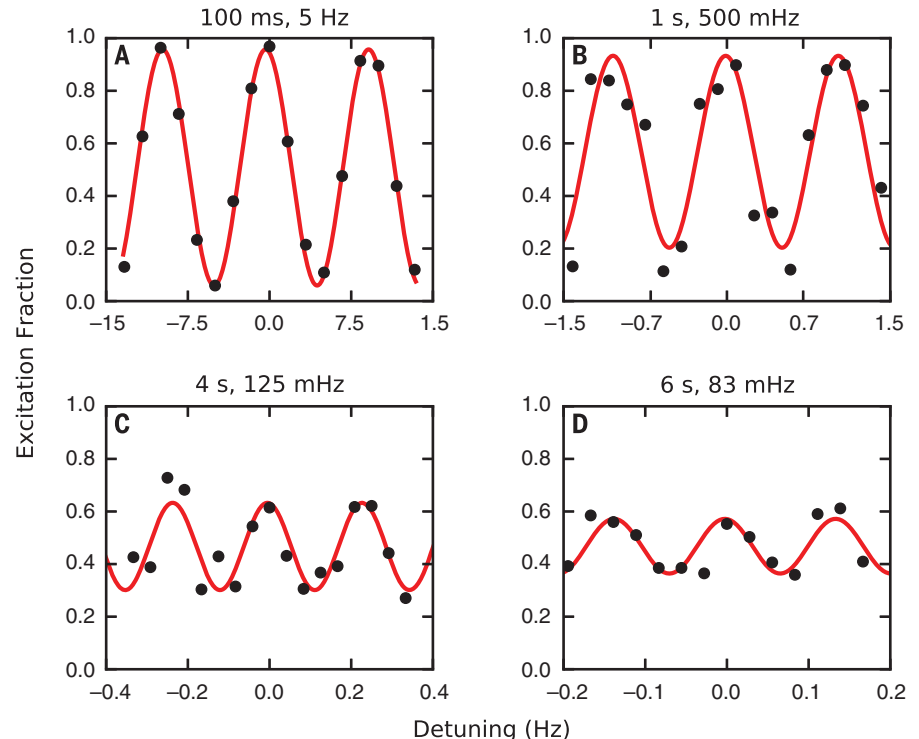


Fig. 3. Narrow-line clock spectroscopy. Ramsey spectroscopy data (black filled circles) taken with 1×10^4 atoms at 15 nK for free evolution times of (A) 100 ms, (B) 1 s, (C) 4 s, and (D) 6 s, using 10-ms $\pi/2$ pulse times. Red lines show sinusoidal fits. With contact interactions and ac Stark shifts controlled in a 3D lattice, we can measure Ramsey fringes at an unprecedented 6-s free evolution time with a density of more than 10^{13} atoms/cm³.

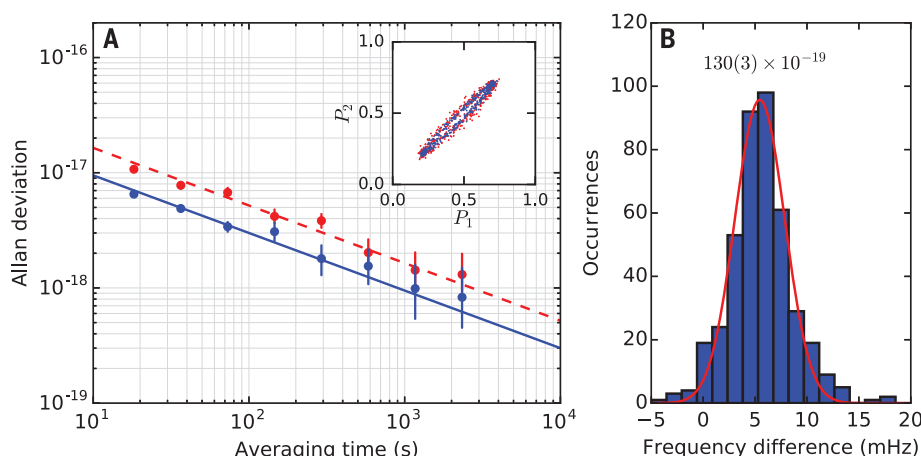


Fig. 4. Synchronous clock comparison. (A) The Allan deviation of the differential frequency shift between two independent regions of the 3D lattice, each having 3000 atoms (blue filled circles). The blue solid line shows an instability of $3.1 \times 10^{-17}/\sqrt{\tau}$. The frequency difference is determined through a Bayesian estimation algorithm that determines the eccentricity of the ellipse of the parametric plot of P_1 versus P_2 (inset, 420 runs). When the number of atoms is reduced to 1000 in each region, the instability increases by $\sqrt{3}$ (red filled circles and red dashed line). The error bars represent 95% confidence intervals, assuming white frequency noise. (B) A histogram of the measured frequency differences for an averaging time of 2.2 hours and 3000 atoms. The fitted Gaussian gives a fractional frequency difference of $129.6(3.5) \times 10^{-19}$.

ensembles in the 3D lattice. The regions, represented by the blue and orange spheres in Fig. 1A, are rectangular cross sections separated from one another by $>6 \mu\text{m}$, each containing 3000 atoms. After a $T_R = 4 \text{ s}$ Ramsey sequence, we performed absorption imaging on the $^1\text{S}_0 \leftrightarrow ^1\text{P}_1$ transition with a $1\text{-}\mu\text{m}$ imaging resolution to independently measure the excitation fractions P_1 and P_2 in the two respective regions. Although most clock shifts are common-mode-suppressed between the two regions, the slightly elliptical polarization of the \hat{z} lattice beam produces a differential vector Stark shift of a few millihertz between the two regions. We measured this effect by probing the $|g; 1/2\rangle \rightarrow |e; 1/2\rangle$ clock transition. The shift manifests itself as a fixed phase between the signals P_1 and P_2 . Plotting P_1 versus P_2 (Fig. 4A, inset) allows us to extract this differential shift in a manner independent of the clock laser noise through either ellipse fitting (45) or Bayesian estimation (46). The QPN is uncorrelated between the two independently detected regions and thus limits the precision of the extracted phase shift. In 2.2 hours of averaging, we measured a shift of $5.56(15) \text{ mHz}$, corresponding to an instability of $3.1 \times 10^{-17}/\sqrt{\tau}$ (Fig. 4A) and a measurement precision of 3.5×10^{-19} (Fig. 4B). To observe the scaling of measurement precision with the number of atoms, we reduced the number of atoms by a factor of 3 and observed an increase in QPN noise by $\sqrt{3}$ (red dashed line in Fig. 4A).

By using larger lattice beam waists, our design can accommodate even greater numbers of atoms, which, combined with reduced preparation time of degenerate gases and increased atomic coherence in the lattice, should enable the operation of synchronous comparisons at better than the $10^{-18}/\sqrt{\tau}$ level, leading to a new generation of

precision measurement tools, including space-based gravitational wave detectors (47). Reaching such performance is extremely challenging for 1D optical lattice clocks, because collisional effects force a compromise between interrogation time and the number of atoms that can be simultaneously interrogated (10, 15).

With quantum-degenerate atoms frozen into a 3D lattice, we can further advance the state of the art in coherent atom-light interactions with the next generation of ultrastable optical reference cavities based on crystalline materials (48–50). Quantum-degenerate clocks also provide a promising platform for studying many-body physics. Future studies of dipolar interactions will not only be necessary for clock accuracy, but will also provide insight into long-range quantum spin systems in a regime distinct from those explored by polar molecules (51, 52), Rydberg gases (53, 54), and highly magnetic atoms (55–58). When clocks ultimately confront the natural linewidth of the atomic frequency reference, degenerate Fermi gases may be useful for engineering longer coherence times through Pauli blocking of spontaneous emission (59) or collective radiative effects (39, 60).

REFERENCES AND NOTES

1. A. Derevianko, M. Pospelov, *Nat. Phys.* **10**, 933–936 (2014).
2. K. Van Tilburg, N. Leeper, L. Bougas, D. Budker, *Phys. Rev. Lett.* **115**, 011802 (2015).
3. A. Arvanitaki, J. Huang, K. Van Tilburg, *Phys. Rev. D* **91**, 015015 (2015).
4. Y. V. Stadnik, V. V. Flambaum, *Phys. Rev. A* **93**, 063630 (2016).
5. A. D. Ludlow, M. M. Boyd, J. Ye, E. Peik, P. Schmidt, *Rev. Mod. Phys.* **87**, 637–701 (2015).
6. T. L. Nicholson et al., *Phys. Rev. Lett.* **109**, 230801 (2012).
7. N. Hinkley et al., *Science* **341**, 1215–1218 (2013).
8. B. J. Bloom et al., *Nature* **506**, 71–75 (2014).
9. I. Ushijima, M. Takamoto, M. Das, T. Ohkubo, H. Katori, *Nat. Photonics* **9**, 185–189 (2015).
10. T. L. Nicholson et al., *Nat. Commun.* **6**, 6896 (2015).
11. C. Grebing et al., *Optica* **3**, 563 (2016).
12. J. Lodewyck et al., *Metrologia* **53**, 1123–1130 (2016).

13. G. K. Campbell et al., *Science* **324**, 360–363 (2009).
14. N. D. Lemke et al., *Phys. Rev. Lett.* **107**, 103902 (2011).
15. M. J. Martin et al., *Science* **341**, 632–636 (2013).
16. T. Akatsuka, M. Takamoto, H. Katori, *Phys. Rev. A* **81**, 023402 (2010).
17. B. DeMarco, D. S. Jin, *Science* **285**, 1703–1706 (1999).
18. R. Jördens, N. Strohmaier, K. Günter, H. Moritz, T. Esslinger, *Nature* **455**, 204–207 (2008).
19. U. Schneider et al., *Science* **322**, 1520–1525 (2008).
20. T. Rom et al., *Nature* **444**, 733–736 (2006).
21. M. Greiner, O. Mandel, T. Esslinger, T. W. Hansch, I. Bloch, *Nature* **415**, 39–44 (2002).
22. Materials and methods are available as supplementary materials.
23. B. J. DeSalvo, M. Yan, P. G. Mickelson, Y. N. Martinez de Escobar, T. C. Killian, *Phys. Rev. Lett.* **105**, 030402 (2010).
24. S. Stellmer, R. Grimm, F. Schreck, *Phys. Rev. A* **87**, 013611 (2013).
25. P. Lemonde, P. Wolf, *Phys. Rev. A* **72**, 033409 (2005).
26. P. G. Westergaard et al., *Phys. Rev. Lett.* **106**, 210801 (2011).
27. M. M. Boyd et al., *Phys. Rev. A* **76**, 022510 (2007).
28. S. Falke et al., *New J. Phys.* **16**, 073023 (2014).
29. C. Shi et al., *Phys. Rev. A* **92**, 012516 (2015).
30. M. Greiner, “Ultracold quantum gases in three-dimensional optical lattice potentials,” thesis, Ludwig-Maximilians-Universität München, Munich, Germany (2003).
31. A. V. Gorshkov et al., *Nat. Phys.* **6**, 289–295 (2010).
32. X. Zhang et al., *Science* **345**, 1467–1473 (2014).
33. F. Scazza et al., *Nat. Phys.* **10**, 779–784 (2014).
34. G. Cappellini et al., *Phys. Rev. Lett.* **113**, 120402 (2014).
35. M. D. Swallows et al., *Science* **331**, 1043–1046 (2011).
36. S. Trotzky et al., *Science* **319**, 295–299 (2008).
37. S. L. Bromley et al., *Nat. Commun.* **7**, 11039 (2016).
38. D. E. Chang, J. Ye, M. D. Lukin, *Phys. Rev. A* **69**, 023810 (2004).
39. S. Krämer, L. Ostermann, H. Ritsch, *Europhys. Lett.* **114**, 14003 (2016).
40. M. Schioppo et al., *Nat. Photonics* **11**, 48–52 (2017).
41. M. Bishof, X. Zhang, M. J. Martin, J. Ye, *Phys. Rev. Lett.* **111**, 093604 (2013).
42. J. G. Dick, in *Proceedings of the 19th Precise Time and Time Interval Applications and Planning Meeting* (1987), pp. 133–147.
43. M. Takamoto, T. Takano, H. Katori, *Nat. Photonics* **5**, 288–292 (2011).
44. C. W. Chou, D. B. Hume, M. J. Thorpe, D. J. Wineland, T. Rosenband, *Phys. Rev. Lett.* **106**, 160801 (2011).
45. G. T. Foster, J. B. Fixler, J. M. McGuirk, M. A. Kasevich, *Opt. Lett.* **27**, 951–953 (2002).
46. J. K. Stockton, X. Wu, M. A. Kasevich, *Phys. Rev. A* **76**, 033613 (2007).
47. S. Kolkowitz et al., *Phys. Rev. D Part. Fields Gravit. Cosmol.* **94**, 124043 (2016).
48. T. Kessler et al., *Nat. Photonics* **6**, 687–692 (2012).
49. G. D. Cole, W. Zhang, M. J. Martin, J. Ye, M. Aspelmeyer, *Nat. Photonics* **7**, 644–650 (2013).
50. D. G. Matei et al., *Phys. Rev. Lett.* **118**, 263202 (2017).
51. B. Yan et al., *Nature* **501**, 521–525 (2013).
52. S. A. Moses et al., *Science* **350**, 659–662 (2015).
53. P. Schaub et al., *Science* **347**, 1455–1458 (2015).
54. H. Labuhn et al., *Nature* **534**, 667–670 (2016).
55. K. Aikawa et al., *Science* **345**, 1484–1487 (2014).
56. A. de Paz et al., *Phys. Rev. A* **93**, 021603 (2016).
57. H. Kadau et al., *Nature* **530**, 194–197 (2016).
58. N. Q. Burdick, Y. Tang, B. L. Lev, *Phys. Rev. X* **6**, 031022 (2016).
59. R. M. Sandner, M. Müller, A. J. Daley, P. Zoller, *Phys. Rev. A* **84**, 043825 (2011).
60. L. Ostermann, H. Ritsch, C. Genes, *Phys. Rev. Lett.* **111**, 123601 (2013).

ACKNOWLEDGMENTS

We thank D. E. Chang and H. Ritsch for insightful discussions on dipolar interactions in a 3D lattice. We also acknowledge technical contributions from and discussions with C. Benko, T. Bothwell, S. L. Bromley, K. Hagen, J. L. Hall, B. Horner, H. Johnson, T. Keep, S. Kolkowitz, J. Levine, T. H. Loftus, T. L. Nicholson, E. Oelker, D. G. Reed, and X. Zhang. This work is supported by NIST, the Defense Advanced Research Projects Agency, the Air Force Office of Scientific Research Multidisciplinary University Research Initiative, and the NSF JILA Physics Frontier Center. G.E.M. is supported by a postdoctoral fellowship from the National Research Council, A.G. is supported by a fellowship from the Japan Society for the Promotion of Science, and L.S. is supported by a National Defense Science and Engineering Graduate Fellowship.

SUPPLEMENTARY MATERIALS

www.sciencemag.org/content/358/6359/90/suppl/DC1
Material and Methods
Figs. S1 to S6
Tables S1 and S2
References (61–63)

7 December 2016; resubmitted 4 June 2017
Accepted 24 August 2017
10.1126/science.aam5538

A Fermi-degenerate three-dimensional optical lattice clock

S. L. Campbell, R. B. Hutson, G. E. Marti, A. Goban, N. Darkwah Oppong, R. L. McNally, L. Sonderhouse, J. M. Robinson, W. Zhang, B. J. Bloom and J. Ye

Science **358** (6359), 90-94.
DOI: 10.1126/science.aam5538

Making a denser optical lattice clock

Some of today's most advanced clocks are made up of large numbers of atoms lined up in a one-dimensional (1D) optical lattice. The numbers improve clock stability, but atomic interactions can limit accuracy. Campbell *et al.* loaded their fermionic strontium atoms into a 3D optical lattice. The low temperatures and strong interactions ensured that the atoms avoided one another, resulting in a neat pattern where each lattice site was occupied by exactly one atom. This ordering reduced the influence of interactions on the clock's accuracy, whereas the high density of atoms enabled by the 3D geometry improved the precision.

Science, this issue p. 90

ARTICLE TOOLS

<http://science.sciencemag.org/content/358/6359/90>

SUPPLEMENTARY MATERIALS

<http://science.sciencemag.org/content/suppl/2017/10/04/358.6359.90.DC1>

REFERENCES

This article cites 58 articles, 10 of which you can access for free
<http://science.sciencemag.org/content/358/6359/90#BIBL>

PERMISSIONS

<http://www.sciencemag.org/help/reprints-and-permissions>

Use of this article is subject to the [Terms of Service](#)

Science (print ISSN 0036-8075; online ISSN 1095-9203) is published by the American Association for the Advancement of Science, 1200 New York Avenue NW, Washington, DC 20005. The title *Science* is a registered trademark of AAAS.

Copyright © 2017 The Authors, some rights reserved; exclusive licensee American Association for the Advancement of Science. No claim to original U.S. Government Works